

1

## 2 **Ratio Limits of Water Storage and Outflow in Rainfall-runoff Process**

3 **Yulong Zhu<sup>a</sup>, Yang Zhou<sup>b</sup>, Xiaorong Xu<sup>c</sup>, Changqing Meng<sup>d</sup>, and Yuankun Wang<sup>e\*</sup>**

4

5 **<sup>a</sup>Yulong Zhu**

6 School of Water Resources and Hydropower Engineering, North China Electric Power University,  
7 Changping Beinong 2# 102206, Beijing, China. Email: [zhuyulong@ncepu.edu.cn](mailto:zhuyulong@ncepu.edu.cn)

8 **<sup>b</sup>Yang Zhou**

9 School of Water Resources and Hydropower Engineering, North China Electric Power University,  
10 Changping Beinong 2# 102206, Beijing, China. Email: [zhouyang@ncepu.edu.cn](mailto:zhouyang@ncepu.edu.cn)

11 **<sup>c</sup>Xiaorong Xu**

12 School of Water Resources and Hydropower Engineering, North China Electric Power University,  
13 Changping Beinong 2# 102206, Beijing, China. Email: [xxrong@ncepu.edu.cn](mailto:xxrong@ncepu.edu.cn)

14 **<sup>d</sup>Changqing Meng**

15 School of Water Resources and Hydropower Engineering, North China Electric Power University,  
16 Changping Beinong 2# 102206, Beijing, China. Email: [els\\_meng@ncepu.edu.cn](mailto:els_meng@ncepu.edu.cn)

17 **<sup>e\*</sup>Yuankun Wang** (Corresponding author)

18 School of Water Resources and Hydropower Engineering, North China Electric Power University,  
19 Changping Beinong 2# 102206, Beijing, China. Email: [yuankunw@ncepu.edu.cn](mailto:yuankunw@ncepu.edu.cn)

20

21 **Abstract**

22 Flash floods typically occur suddenly within hours of heavy rainfall. Accurate forecasting of flash floods in  
23 advance using the two-dimensional (2D) shallow water equations (SWEs) remains a challenge, due to the  
24 governing equations of SWEs being difficult-to-solve partial differential equations (PDEs). Aiming at  
25 shortening the computational time and gaining more time for issuing early warnings of flash floods, a new  
26 relationship between water storage and outflow in the rainfall-runoff process is attempted to be constructed  
27 by assuming the catchment as a water storage system. Through numerical simulations of the diffusion wave  
28 (DW) approximation of SWEs, the water storage and discharge are found to be limited to envelope lines, and  
29 the discharge/water depth process lines during water rising and falling showed a grid-shaped distribution.  
30 Furthermore, if a catchment is regarded as a semi-open water storage system, there is a nonlinear relationship  
31 between the inside average water depth and the outlet water depth, namely the water storage ratio curve,  
32 which resembles the shape of a “plume”. In the case of an open channel without considering spatial  
33 variability, the water storage ratio curve is limited to three values (i.e., the upper, the steady, and the lower  
34 limit), which are found to be independent of meteorological (rainfall intensity), vegetation (Manning’s  
35 coefficient), and terrain (slope gradient) conditions. Meteorological, vegetation, and terrain conditions only  
36 affect the size of the “plume” without changing its shape. Rainfall, especially weak rain (i.e. when rainfall  
37 intensity is less than  $5.0 \text{ mm h}^{-1}$ ) significantly affects the fluctuations of the water storage ratio, which can be  
38 divided into three modes, that is Mode I (inverse S-shape type) during the rainfall beginning stage, Mode II  
39 (wave type) during the rainfall duration stage, and Mode III (checkmark type) during rainfall end stage.  
40 Results indicate that the determination of the nonlinear relationship of the water storage ratio curve under  
41 different geographical scenarios will provide new ideas for simulation and early warning of flash floods.

42

## 43 1. Introduction

44 Flood disaster is a significant global health and economic threat. Disastrous floods have caused millions  
45 of fatalities in the twentieth century and billions of dollars in direct economic losses each year (Merkuryeva,  
46 et al., 2015; Merz, et al., 2021; Ruidas, et al., 2022). According to statistics (Lee, et al., 2020), from 2001 to  
47 2018, over 2,900 floods caused over 93,000 deaths and over 490 billion USD in economic damages  
48 worldwide. Based on 250-meter resolution daily satellite images of 913 major flood events during the same  
49 period, the total area inundated by floods is estimated to be 2.23 million km<sup>2</sup> and the directly affected  
50 population is estimated to be 255 to 290 million (Tellman, et al., 2021). With the influence of climate change  
51 and extreme El Niño events (Ward, et al., 2014; Cai, et al., 2014), flood events caused by extreme  
52 precipitation are occurring frequently in many regions around the world (Kirezci, et al., 2020; Najibi and  
53 Devineni, 2018; Almazroui, 2020). From 2020 to 2023, catastrophic floods caused by several extreme  
54 rainfall events were reported in Germany (Tradowsky, et al., 2023), China (Hsu, et al., 2021), Italy (Valente,  
55 et al., 2023), Japan (Kobayashi, et al., 2023), Pakistan (Nanditha, et al., 2023) and other developed or  
56 developing countries and regions, even in some desert areas, e.g. in the Taklimakan Desert and the Atacama  
57 Desert, as reported by Li and Yao (2023) and by Cabré et al. (2023) respectively. Research show that under a  
58 high emissions scenario, in latitudes above 40° north, compound flooding could become more than 2.5 times  
59 as frequent by 2100 compared to the present (Bevacqua, et al., 2020). It means that in the future, the fraction  
60 of the global population at risk of floods will be growing.

61 Flood simulation provides an effective means of flood forecasting to reduce property and life losses in  
62 flood-threatened areas around the world. Particularly, weather prediction-based distributed  
63 hydrological/hydraulic models are considered to be an effective strategy for flood simulation (Ming, et al.,  
64 2020). Hence, a large number of scholars are committed to improving the simulation efficiency or simulation

65 accuracy of distributed hydrological/hydraulic models. Accordingly, they have developed many forms of  
66 hydrological models and hydrodynamic models in the past decades. Among them, the hydrological models  
67 include Stanford Watershed Model IV-SWM (Crawford and Linsley, 1966), SHE/MIKESHE model (Abbott,  
68 et al., 1986), Tank model (Sugawara, 1995), Soil and Water Assessment Tool-SWAT (Arnold and Williams,  
69 1987), and TOPMODEL (Beven and Kirkby, 1979), etc. The hydrodynamic models include the  
70 one-dimensional (1D) Saint-Venant equation (Köhne, et al., 2011), the two-dimensional (2D) SWEs  
71 (Camassa, et al., 1994), and the three-dimensional (3D) integrated equations of runoff and seepage (Mori, et  
72 al., 2015). In addition, a variety of hydrological-hydrodynamic coupling models have also been proposed by  
73 Kim, et al. (2012); Liu, et al. (2019); Hoch, et al. (2019), and other scholars. Particularly, SWEs are the main  
74 governing equations for simulating floods. However, flood simulation based on SWEs is a time-consuming  
75 process due to its governing equations being a hyperbolic system of first-order nonlinear partial differential  
76 equations (PDEs) (Li and Fan, 2017). Therefore, many scholars attempted to improve the efficiency and  
77 accuracy of flood simulation through computer technology e.g. applying GPU parallel computing (Crossley,  
78 et al., 2010) or advanced numerical scheme (Sanders, et al., 2010). For hydrological studies, the performance  
79 of hydrological modeling is usually challenged by model calibration and uncertainty analysis during  
80 modeling exercises (Wu, et al., 2021).

81 Efficient and stable solution of the hydrodynamic model has long been an important issue in flood  
82 forecasting. Since the SWEs are nonlinear hyperbolic PDEs, the increase in the calculation domain and the  
83 increase in the degree of discreteness will greatly increase the difficulty of solving SWEs. In addition, when  
84 using high-resolution terrain to improve model calculation accuracy, non-physical phenomena such as false  
85 high flow velocity in steep terrain will also occur, resulting in calculation distortion and a sharp increase in  
86 calculation time. Hence, we try to ignore the complex exchange/transfer process of mass and momentum

87 (hydrodynamic models), and also abandon the empirical relationships (hydrological models) between the  
 88 input (precipitation), the transmission (flow rate), and the output (discharge) in the catchment area. A  
 89 catchment is regarded as a semi-open water storage system, and the complex problem is simplified into three  
 90 megascopic variables, i.e., inflow, water storage, and outflow. For one watershed, the complex internal flow  
 91 processes could be ignored if the physical mechanism between inflow, water storage, and outflow can be  
 92 found under different meteorological, geographical, and geological conditions. In other words, if we can give  
 93 a physical-based relationship between the three megascopic variables, flood forecasting will become much  
 94 simpler. For this goal, a “plume” shaped nonlinear relationship between the inside average water depth and  
 95 the outlet water depth, namely the water storage ratio curve, was found by using the calculation results of the  
 96 hydrodynamic model.

## 97 2. Methods

98 An arbitrary catchment (Fig. 1b) could be assumed to be a conceptual water tank (Fig. 1a). In this water  
 99 tank, according to the law of conservation of mass, the complex confluence process of surface runoff could  
 100 be neglected and it can be described only by the relationship between input, storage and output, which can be  
 101 expressed as Eq. 1,

$$102 \quad \underbrace{A \times \frac{dH}{dt}}_{storage} = \underbrace{R \times A}_{rainfall} - \underbrace{I \times A}_{infiltration} + \underbrace{F \times A}_{exfiltration} - \underbrace{E \times A}_{evaporation} - \underbrace{\frac{Q}{A} \times A}_{discharge} \quad (1)$$

103 where  $A$  is catchment area ( $m^2$ );  $t$  is time (s);  $H$  is internal average water depth (m);  $R$  is rainfall  
 104 intensity ( $m s^{-1}$ );  $I$  is infiltration ( $m s^{-1}$ );  $F$  is exfiltration ( $m s^{-1}$ );  $E$  is evaporation ( $m s^{-1}$ ) and  $Q$  is discharge  
 105 ( $m^3 s^{-1}$ ).

106 In this section, attentions are focused on the surface flow of runoff, so the runoff-atmosphere moisture  
 107 exchange (evaporation) and runoff-soil moisture exchange (infiltration and/or exfiltration) are

108 non-considered. Zhu et al. (2020) validated the effectiveness of a diffusion wave (DW) approximation of  
 109 shallow water equations by numerical simulations for simulating ground surface runoff,

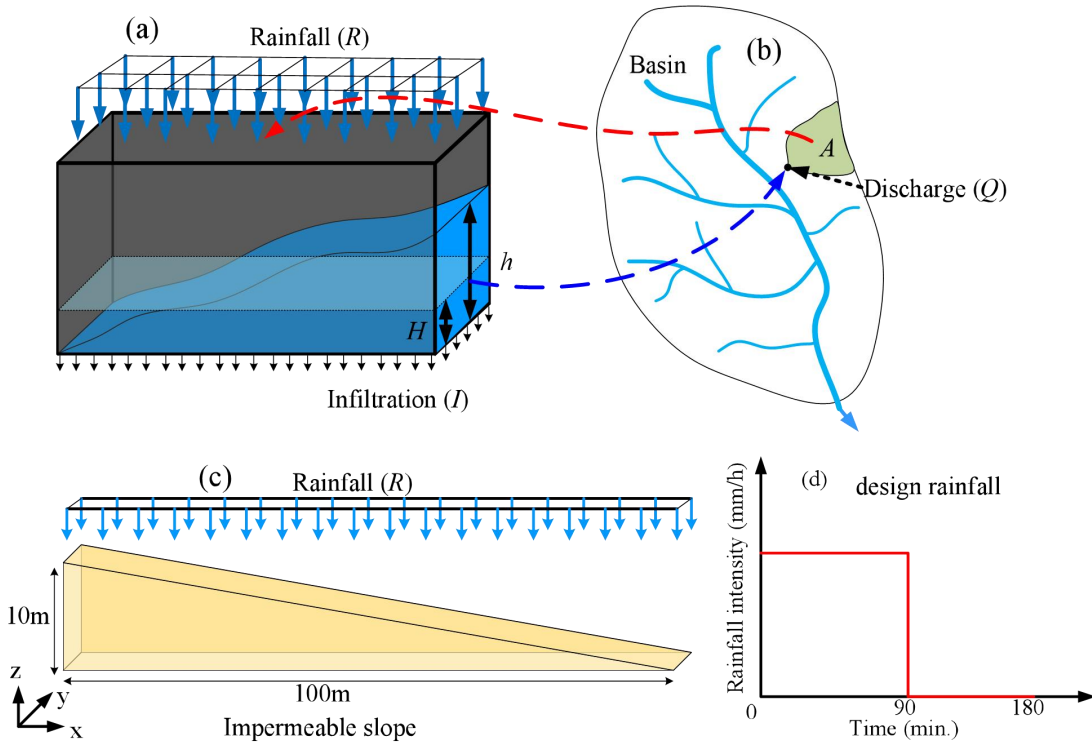
$$110 \quad \frac{\partial h}{\partial t} - \nabla \left( \frac{h^{5/3}}{n_m \sqrt{|S|}} \nabla (h + z) \right) = R \quad (2)$$

111 where  $h$  is water depth (m);  $z$  is elevation (m);  $n_m$  is Manning's coefficient ( $\text{s m}^{-1/3}$ ) and  $S$  is the slope  
 112 gradient.

113 To improve the computational efficiency of the hydrodynamic model, after strict mathematical  
 114 derivation according to the basic hydrodynamic equation and the law of conservation of mass, Zhu et al.  
 115 (2022) proposed a hydrological-hydrodynamic integrated model, i.e., distributed runoff model (DRM) as,

$$116 \quad \begin{cases} \frac{dH}{dt} = R - q \\ H = \eta h = \eta \left( \frac{n_m}{\sqrt{S}} \right)^{0.6} q^{0.6} \left( \frac{A}{B} \right)^{0.6} \end{cases} \quad (3)$$

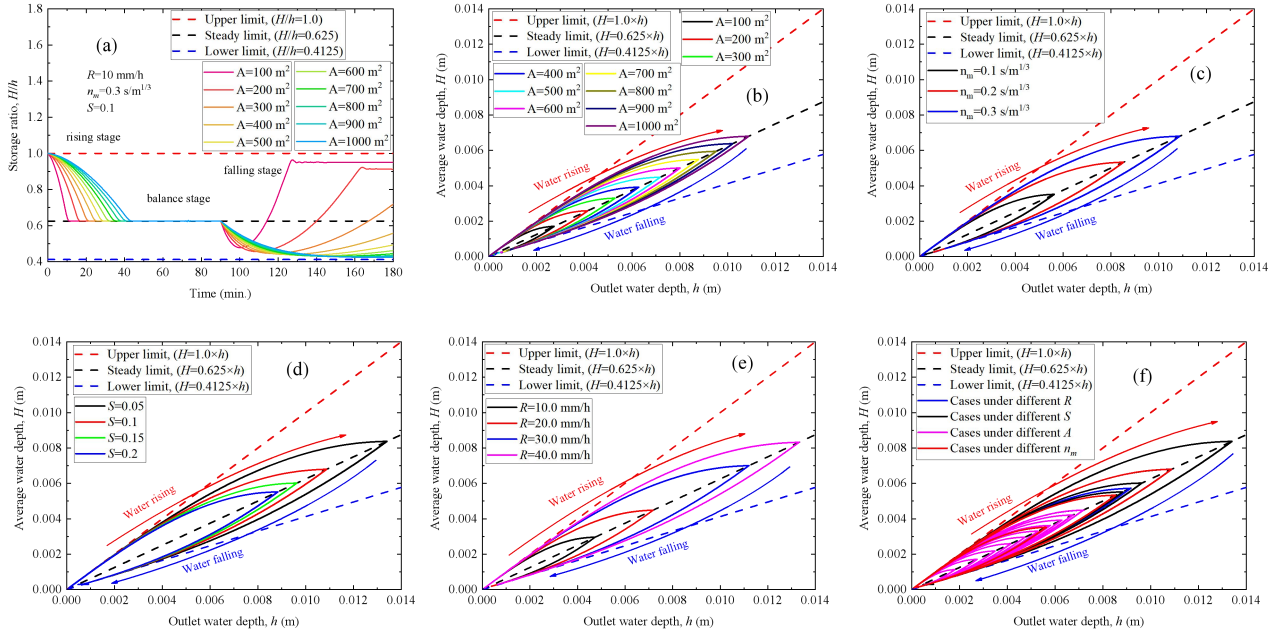
117 where  $q=Q/A$  is conceptual outflow ( $\text{m s}^{-1}$ );  $\eta$  is the water storage ratio;  $B$  is the outlet width (m).



118  
 119 **Fig. 1. Conceptual schematic of the DRM and numerical model.** (a) conceptual water tank; (b)  
 120 conceptual catchment; (c) impermeable conceptual slope model; (d) design rainfall.

### 121 3. Limits and “plume” shape of water storage ratio curve

122 The conceptual hydrological model takes the inside average water depth ( $H$ ) in the catchment area as  
123 the independent variable (Eq. 1). However, the hydrodynamic equations take the water depth at any outlet ( $h$ )  
124 as an independent variable (Eq. 2). If a relationship between the inside average water depth ( $H$ ) and outlet  
125 water depth ( $h$ ) can be established, then this relationship will have both hydrodynamic and hydrological  
126 characteristics. Therefore, to find the  $H$ - $h$  relationship, an impermeable conceptual slope model was built as  
127 shown in Fig. 1c, and numerical simulations were performed using diffusion wave (DW) approximation (Eq.  
128 2) of shallow water equations (SWEs). The water storage ratio is defined as the inside average water depth  
129 ( $H$ ) divided by the outlet water depth ( $h$ ). Firstly, the numerical simulations are performed under a designed  
130 rainfall condition, i.e., rainfall intensity is  $10 \text{ mm h}^{-1}$  and rainfall duration is 90 minutes with a total time of  
131 180 minutes as shown in Fig. 1d. From the time-dependent water storage ratio ( $H/h$ ) under different  
132 catchment area (Fig. 2a), it can be seen that the continuous rainfall will cause the water storage ratio ( $H/h$ ) to  
133 gradually decrease from the initial value 1.0 (upper limit) to a stable value, which is approximately 0.625  
134 (steady limit). When the rainfall ends, the value of the water storage ratio ( $H/h$ ) decreases first and then  
135 increases, showing a U-shaped curve with a lower limit, which is approximately 0.4125. Afterward, the  
136 water storage ratio curves under ten kinds of catchment area (Fig. 2b), three kinds of Manning’s coefficient  
137 (Fig. 2c), four kinds of slope gradient (Fig. 2d), and four kinds of rainfall intensity (Fig. 2e) conditions are  
138 obtained from parametric analyses and collected in Fig. 2f.



139

140

141

**Fig. 2. Water storage ratio curves.** (a) time-dependent water storage ratio under different catchment

142

areas with  $10 \text{ mm h}^{-1}$ ; (b) water storage ratio curves under ten kinds of catchment area; (c) water storage ratio

143

curves under three kinds of Manning's coefficient; (d) water storage ratio curves under four kinds of slope

144

gradient; (e) water storage ratio curves under four kinds of rainfall intensity; (f) collection of the above

145

twenty one water storage ratio curves. Three limit lines envelop all water storage ratio curves, i.e., upper

146

limit ( $H/h=1.0$ ), steady limit ( $H/h=0.625$ ), and lower limit ( $H/h=0.4125$ ).

147

Finally, it is found that water storage ratio curves resemble the shape of a “plume”. When the water

148

outlet depth is the same, the water storage ratio ( $H/h$ ) of the water-rising limb is higher than that of the

149

water-falling limb. Furthermore, in the case of an open channel without considering spatial variability, there

150

are three limits (the upper, the steady, and the lower limit) of the water storage ratio curves, which are found

151

to be independent of meteorological (rainfall intensity), vegetation (Manning's coefficient), and terrain (slope

152

gradient) conditions. Meteorological, vegetation, and terrain conditions only affect the size of the “plume”

153

without changing its shape which is anchored by three limits. This means that the three limits and the water

154

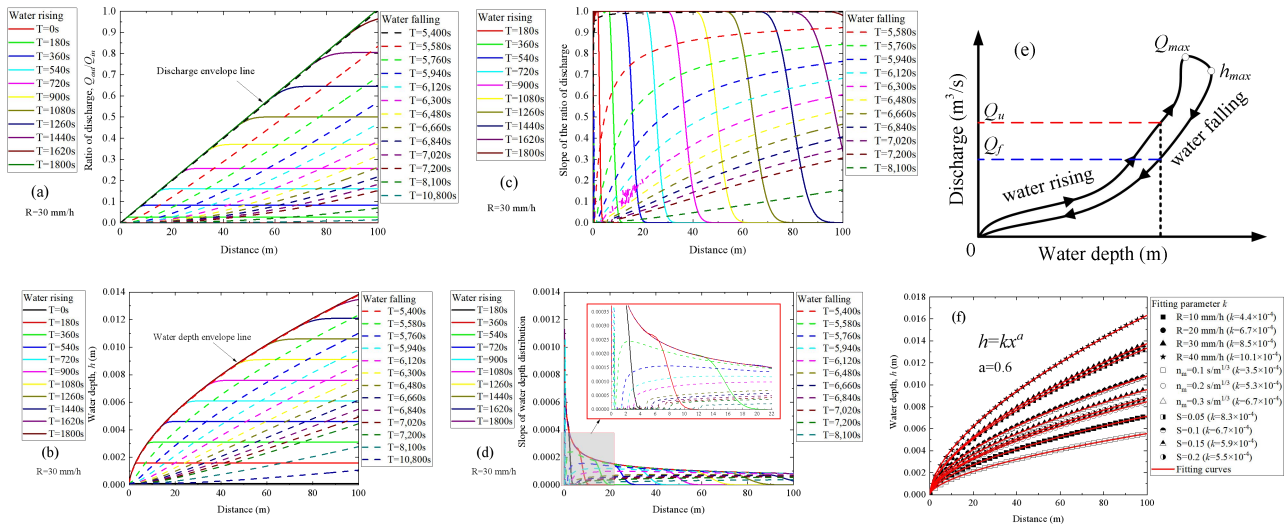
storage ratio curves provide a key to establishing a relationship between the hydrodynamic models and the

155 hydrological models.

156 **4. Grid-shaped cross-distribution of discharge/water depth process lines during water rising and**  
157 **falling**

158 To obtain further insights into the causes for the formation of the water-rising limb and the water-falling  
159 limb of the water storage ratio curve, the ratio of discharge (i.e., the ratio of the total outflows ( $Q_{out}$ ) to the  
160 total inflows ( $Q_{in}$ )), and the water depth ( $h$ ) along the slope are discussed in Fig. 3a and Fig. 3b, respectively.  
161 Results indicate that there is an envelope line that controls the distribution of the discharge and water depth  
162 along the slope, respectively. The discharge envelope line is a straight line with a slope of 1.0 (Fig. 3a), while  
163 the water depth envelope line is a nonlinear curve controlled by a power function of general form  $h=kx^a$  (Fig.  
164 3b). It means that if the duration of rainfall with a constant intensity is long enough, the catchment system  
165 will eventually reach an equilibrium state between inflow and outflow.

166 On the other hand, the process lines of discharge and water depth during water rising and falling present  
167 a grid-shaped cross-distribution (Fig. 3a and Fig. 3b). Similarly, from the view of the gradient of the  
168 discharge and water depth process lines during water rising and falling, the discharge gradient curves (Fig. 3c)  
169 and the water depth gradient curves (Fig. 3d) also present a grid-shaped cross-distribution during water rising  
170 and falling, which might be the cause of the looped rating curve (Fig. 3e), i.e., higher discharges for the  
171 rising limb ( $Q_u$ ) than for the recession limb ( $Q_f$ ) at the same stage (Petersen-Øverleir, 2006). After fitting the  
172 value of parameter  $k$  and  $a$  under different rainfall intensity ( $R$ ), Manning's coefficient ( $n_m$ ), and slope  
173 gradient ( $S$ ) conditions (Fig. 3f), it is found that the parameter  $a$  is a constant, while the change of parameter  
174  $k$  is positively correlated with the change of rainfall intensity ( $R$ ) and Manning's coefficient ( $n_m$ ), but  
175 negatively correlated with the change of slope gradient ( $S$ ).



176

177

178

179

180

181

182

183

184

185

186

187

188

189

190

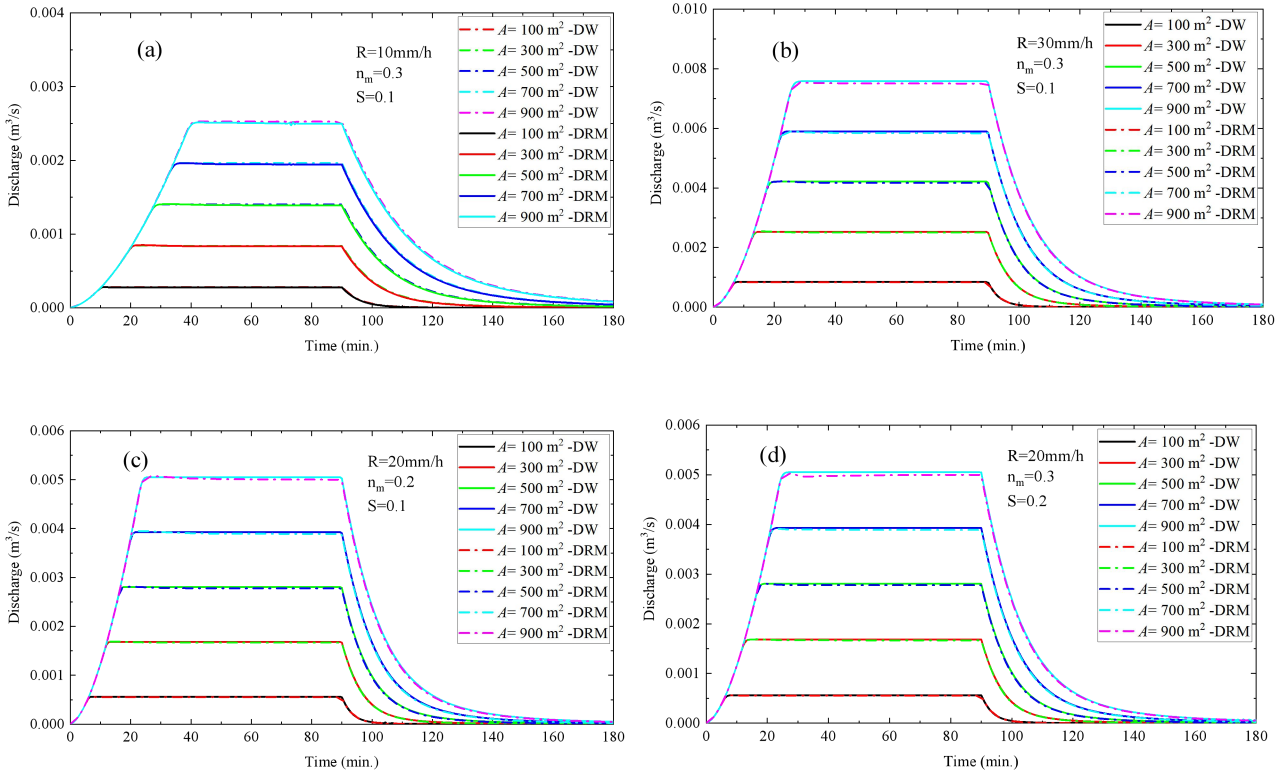
191

192

**Fig. 3. Discharge/water depth process lines during water rising and falling.** (a) discharge process lines during water rising and falling; (b) gradient lines of discharge process line during water rising and falling; (c) schematic diagram of looped rating curve; (d) water depth process lines during water rising and falling; (e) gradient lines of water depth process lines during water rising and falling; (f) change of water depth envelope line under different rainfall intensity ( $R$ ), Manning's coefficient ( $n_m$ ), and slope gradient ( $S$ ).

Based on the water storage ratio curve, a hydrological-hydrodynamic integrated model, namely the Distributed Runoff Model (DRM), is established with the governing equations in Eq. 3. To check the effectiveness and applicability of DRM, a comparative analysis of the numerical results obtained from the DRM and the DW model is implemented. We found that the DRM quickly reproduces the calculation results of the time-consuming DW model under different rainfall intensities (Fig. 4a and Fig. 4b), different Manning's coefficient, and different slope gradients (Fig. 4c and Fig. 4d). meaning that the water storage ratio curve will provide new ideas for simulation and early warning of floods. In addition, due to the governing equations of DRM being an ordinary differential equations (ODEs), the computational efficiency of DRM is much higher than the DW model, which is governed by nonlinear partial differential equations (PDEs). More attention should be paid to the determination of the nonlinear relationship of the water storage

193 ratio curve under different geographical scenarios, which will be beneficial to the proposal of more efficient  
 194 flood forecasting methods or early warning systems.



195

196

197 **Fig. 4. Comparative analyses of discharge calculated by DW and DRM under designed rainfall.** (a)  
 198 controlled group; (b) compared with (a), only the rainfall intensity is changed; (c) compared with (a), rainfall  
 199 intensity and Manning coefficient are changed; (d) compared with (a), rainfall intensity and slope gradient  
 200 are changed.

201 **5. Validation of DRM by considering infiltration calculated by Horton infiltration method.**

202 In the above section, the simulations of DW and DRM are based on an impermeable conceptual slope  
 203 model as shown in Fig. 1c. After considering infiltration in the DW and DRM, the Eq. 2 and Eq. 3 become:

204 
$$\frac{\partial h}{\partial t} - \nabla \left( \frac{h^5}{n_m \sqrt{|S|}} \nabla (h + z) \right) = R - I \quad (4)$$

205 
$$\begin{cases} \frac{dH}{dt} = R - q - I \\ H = \eta h = \eta \left(\frac{n_m}{\sqrt{S}}\right)^{0.6} q^{0.6} \left(\frac{A}{B}\right)^{0.6} \end{cases} \quad (5)$$

206 Infiltration ( $I$ ) is calculated by Horton's infiltration model (Horton, 1933), which suggests an  
 207 exponential equation for modeling the soil infiltration capacity  $f_p$  ( $\text{m s}^{-1}$ ):

208 
$$f_p(t) = f_c + (f_0 - f_c)e^{-kt} \quad (6)$$

209 where  $f_0$  is the initial infiltration capacities ( $\text{m s}^{-1}$ ),  $f_c$  is the final infiltration capacities ( $\text{m s}^{-1}$ ),  $k$   
 210 represents the rate of decrease in the capacity ( $\text{s}^{-1}$ ). The infiltration parameter sets are listed in Table 1.

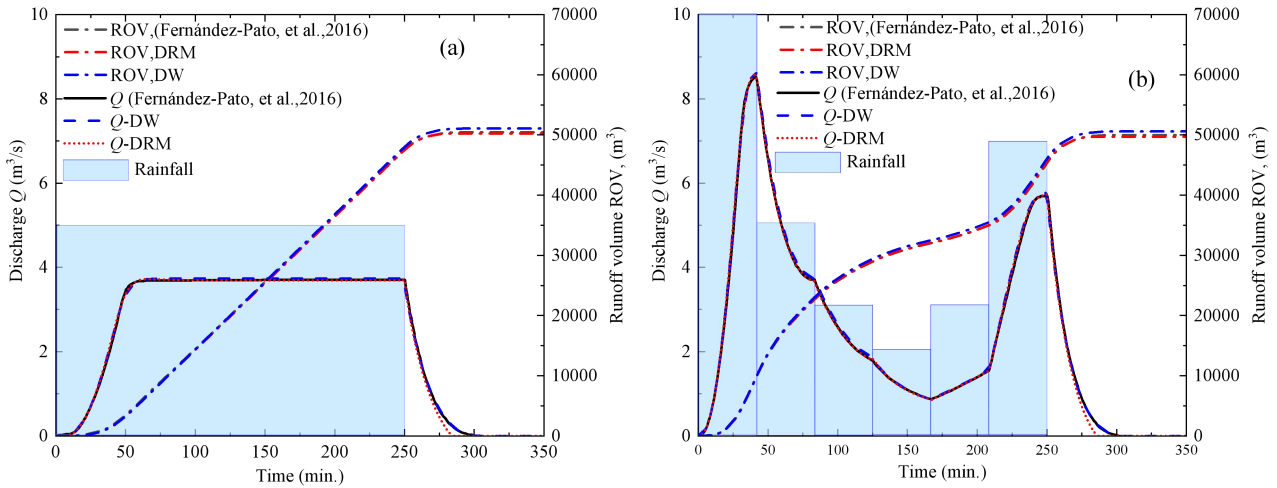
212 **Table 1** Infiltration parameter sets.

Parameter	$k$ ( $\text{s}^{-1}$ )	$f_c$ ( $\text{m s}^{-1}$ )	$f_p$ ( $\text{m s}^{-1}$ )
Value	$2.43 \times 10^{-3}$	$3.272 \times 10^{-5}$	$1.977 \times 10^{-4}$

213 A rainfall event begins with a weak precipitation intensity. When the rainfall intensity is less than the  
 214 infiltration capacity, all the rainwater will infiltrate into the soil. While, when the rainfall intensity exceeds  
 215 the soil infiltration capacity, the surface water is generated, and Horton law (Eq. 6) applies:

216 
$$I = \begin{cases} R(t) & \text{if } R(t) \leq f_p(t) \\ f_p(t) & \text{if } R(t) > f_p(t) \end{cases} \quad (7)$$

217 Results of outlet discharge ( $Q$ ) and runoff volume (ROV) calculated by DW and DRM are compared  
 218 with the reference results adopted from Fernández-Pato et al., (2016) as shown in Fig. 5. Fig. 5a shows the  
 219 comparison of results under a uniform design rainfall. In this case, the rain volume is  $75,000 \text{ m}^3$  with a  
 220 duration of 250 minutes (min.). Fig. 5b shows the comparison of results under a non-uniform rainfall. Rain  
 221 volume is  $75,000 \text{ m}^3$  with a duration of 250 minutes (min.). From Fig. 5, it can be recognized that after  
 222 considering infiltration, except that the calculation results of DRM are a little small at the end-stage of  
 223 rainfall, the calculation results of DRM are still highly consistent with the calculation results of the DW  
 224 model and reference results adopted from Fernández-Pato et al., (2016).



225

226

**Fig. 5. Outlet discharge ( $Q$ ) and runoff volume (ROV) calculated by DW and DRM vs. reference**

227

**results adopted from Fernández-Pato et al., (2016).**

228

## 6. Fluctuation of water storage ratio under natural rainfall conditions

229

After implementing a real rainfall event in the impermeable conceptual slope model (Fig. 1c), the

230

change of the water storage ratio is calculated as shown in Fig. 6. Rainfall data was recorded from 09 August

231

2022 00:00 - 10 August 2022 00:00 in Aomori Prefecture, Japan and 29 August 2016 01:00 - 31 August 2016

232

09:00 in Nissho Pass, Japan (<https://www.data.jma.go.jp>). The total simulation time is 30 hours and 56 hours,

233

respectively. Results show that in addition to the fluctuations of water storage ratio in the beginning and end

234

stages of rainfall, there are mainly ten fluctuation periods of water storage ratio during the rainfall duration

235

stage, identified as 1<sup>#</sup>, 2<sup>#</sup>, 3<sup>#</sup>, 4<sup>#</sup>, and 5<sup>#</sup> in Fig. 6a and 6<sup>#</sup>, 7<sup>#</sup>, 8<sup>#</sup>, 9<sup>#</sup>, and 10<sup>#</sup> in Fig. 6b. The fluctuations are

236

found to be mainly caused by weak rainfall (i.e. rainfall intensity is near  $5.0 \text{ mm h}^{-1}$ ) as pointed by the red

237

arrows in Fig. 6a and Fig. 6b. The magnitude of the fluctuations appears to be positively correlated with the

238

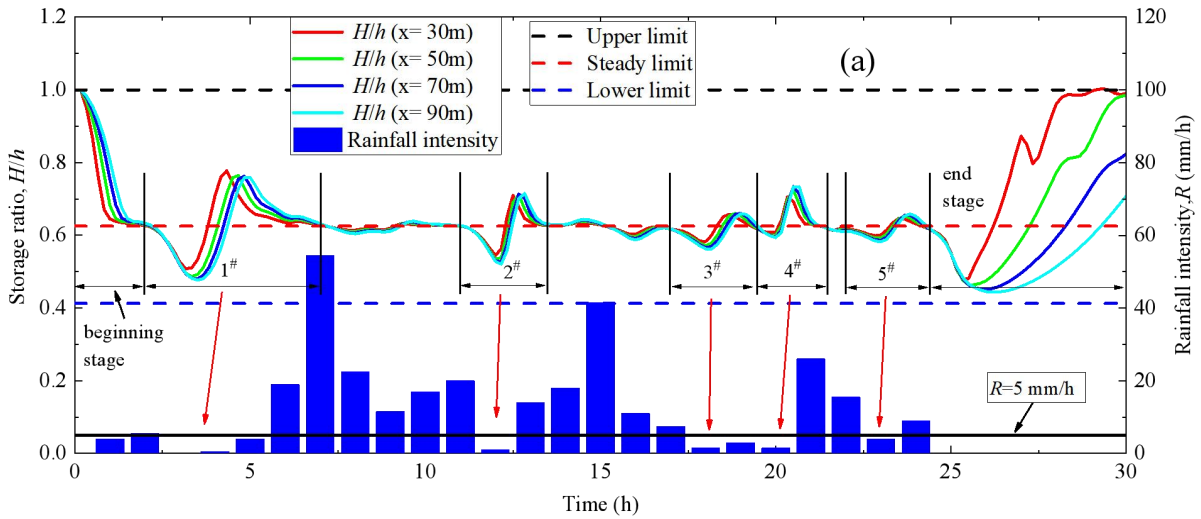
difference between rainfall intensity and  $5.0 \text{ mm h}^{-1}$ . When the rainfall intensity continues to be greater than

239

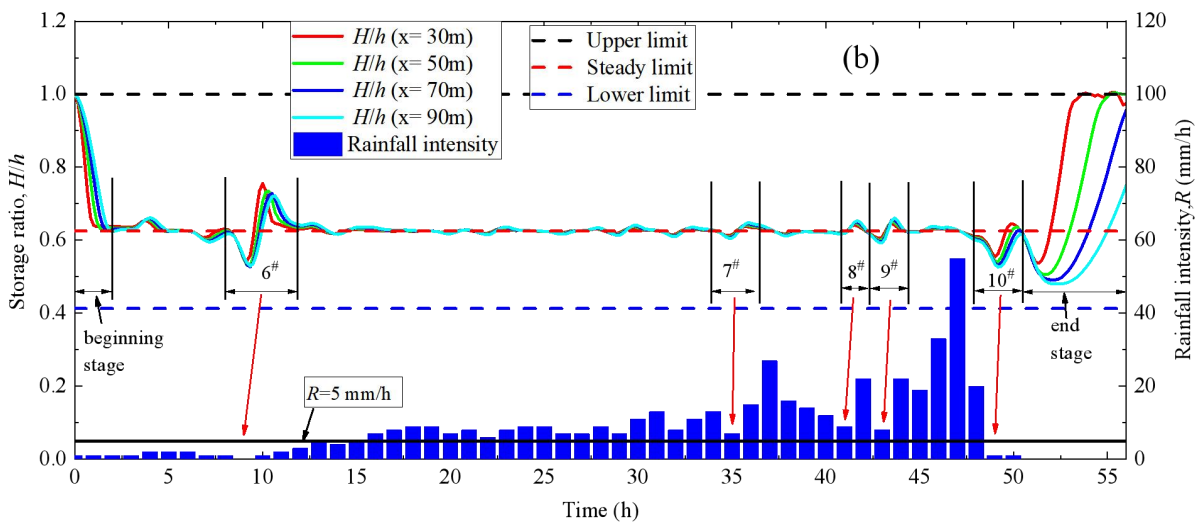
$5.0 \text{ mm h}^{-1}$ , the fluctuation of of water storage ratio is not obvious. The water storage ratio is stable near the

240

steady limit, even if there is heavy rainfall during this period.



241



242

243 **Fig. 6. The fluctuation of water storage ratio and the effectiveness of DRM in natural rainfall events. (a)**

244

Aomori Prefecture; (b) Nissho Pass.

245

Besides, the fluctuations of the water storage ratio can be divided into three modes, that is Mode I

246

identified as the inverse S-shape type during the rainfall beginning stage (Fig. 7a), Mode II identified as

247

wave type during the weak rainfall duration stage (Fig. 7b), and Mode III identified as checkmark type

248

during rainfall end-stage (Fig. 7c). Among them, Mode I is that the water storage ratio drops from upper limit

249

to steady limit in an inverse S-shape. Mode II is that the water storage ratio fluctuates around the steady limit.

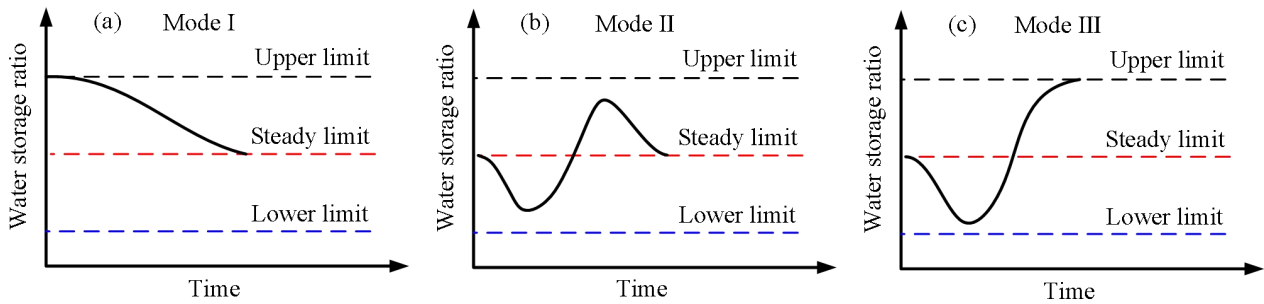
250

Mode III is that the water storage ratio first drops from the steady limit to the lower limit and then rises to the

251

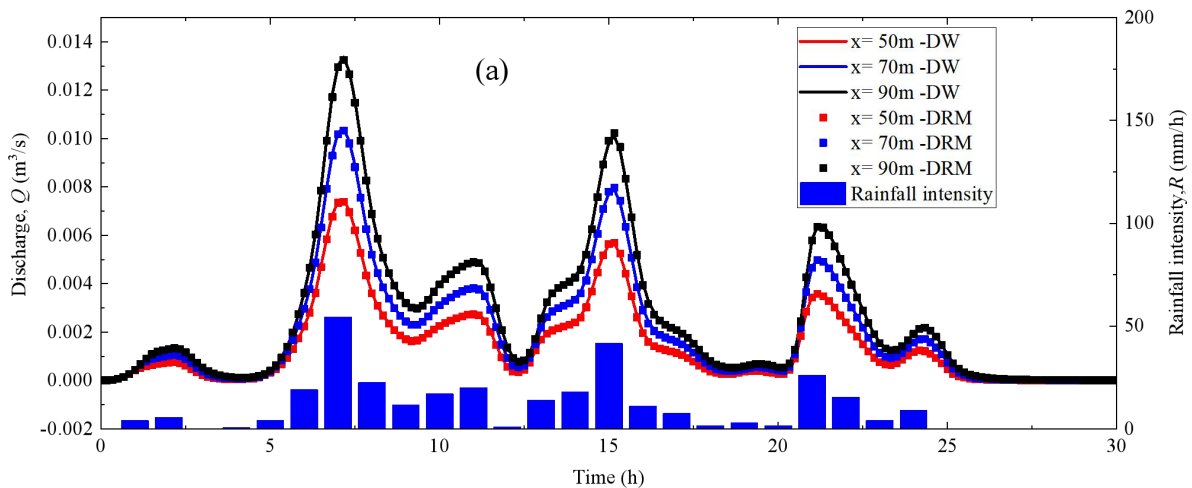
upper limit. This means that the certainty of the fluctuation modes will provide the possibility for

252 quantitative analysis of the fluctuation of the water storage ratio induced by the change in the rainfall  
 253 intensity.

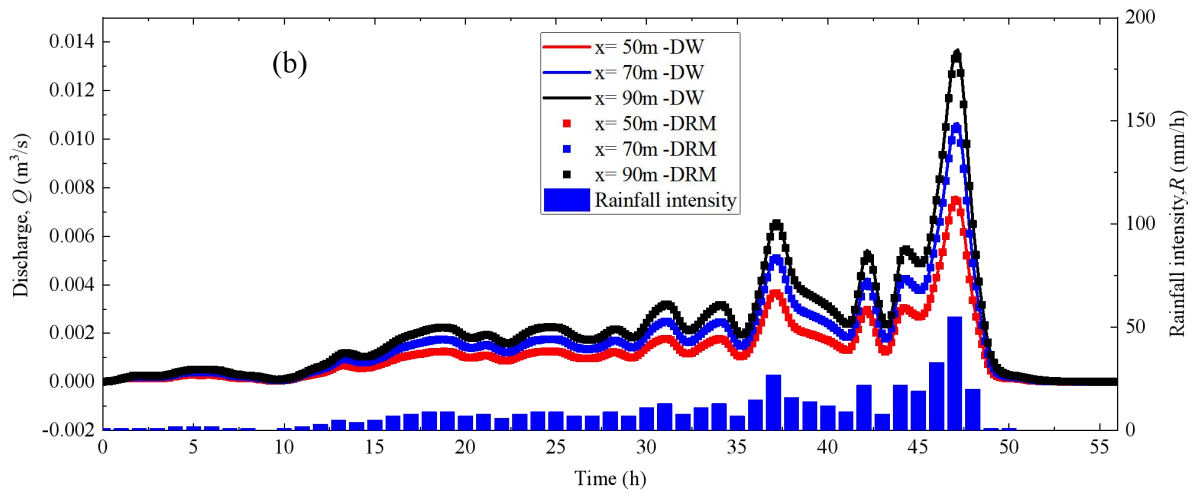


254  
 255 **Fig. 7. Three kinds of water storage ratio fluctuation modes in natural rainfall events.** (a) Mode I during  
 256 the rainfall beginning stage; (b) Mode II during the weak rainfall duration stage; (c) Mode III during the  
 257 rainfall end stage.

258 Figures 8a and 8b show the simulation results of discharge calculated by the DRM and DW model using  
 259 the rainfall data recorded in Aomori Prefecture and Nissho Pass, Japan, respectively. Results suggest that  
 260 after the determination of the water storage ratio fluctuations, the calculation results of DRM are in good  
 261 agreement with those of the DW model, meaning that DRM provides a new and more effective theoretical  
 262 scheme for flood prediction.



263



264

265 **Fig. 8. Time-dependent discharge calculated by DRM and DW model. (a) Aomori Prefecture; (b) Nissho**

266

Pass.

267 **7. Discussions and Conclusions**

268 Based on a conceptual slope model, numerical simulations of the rainfall-runoff process are performed  
 269 by using the diffusion wave (DW) approximation of SWEs. A “plume” shaped nonlinear relationship  
 270 between water storage and outflow, defined as the water storage ratio, is found between the inside average  
 271 water depth and the outlet water depth in a catchment. The water storage ratio is controlled by three limits,  
 272 namely upper limit, steady limit, and lower limit with the value of approximately 1.0, 0.625, and 0.4125,  
 273 respectively. Under the control of the three limits, meteorological, vegetation, and terrain conditions only  
 274 affect the size of the “plume” without changing its shape. The regular curve shape of the water storage ratio  
 275 provides the possibility to construct a correlation between the water storage in the catchment area and the  
 276 outlet discharge.

277 Based on the water storage ratio, a hydrological-hydrodynamic integrated model-DRM, is established,  
 278 which shows high calculation accuracy and computational efficiency. This is because the governing  
 279 equations of DRM are ordinary differential equations (ODEs), which are much easier to solve than nonlinear

280 partial differential equations (PDEs). However, the calculations of DRM and DW only involve the  
281 confluence part of surface water and infiltration. While the interbasin groundwater flow as inputs to the  
282 watershed (exfiltration) and evaporation are not considered, this is inconsistent with the real rainfall-runoff  
283 process in the watershed and may lead to deviations in the calculation results. Therefore, the flow exchange  
284 between surface water and groundwater during the existence and extinction of runoff also needs to be further  
285 realized by establishing a dynamic coupling model of surface water and groundwater.

286 In addition, the water storage and discharge are limited to envelope lines, and the discharge/water depth  
287 process lines during water rising and falling showed a grid-shaped distribution, which might be the cause of  
288 the looped rating curve, i.e., higher discharges for the rising limb than for the recession limb at the same  
289 stage. Rainfall, especially weak rainfall (i.e. rainfall intensity is less than  $5.0 \text{ mm h}^{-1}$ ) significantly affects the  
290 fluctuations of water storage ratio. The fluctuations of water storage ratio during a real rainfall event can be  
291 divided into three modes, that is Mode I identified as inverse S-shape type during the rainfall beginning stage,  
292 Mode II identified as Wave type during weak rainfall duration stage, and Mode III identified as checkmark  
293 type during rainfall end stage. It is worth noting that a qualitative determination of the three fluctuation  
294 modes of water storage ratio during rainfall events is obtained, but the quantitative analysis still needs to be  
295 further carried out in the future.

296 The findings in this study provide a key to establishing a simpler prediction model for flash floods. The  
297 water storage ratio has been proven to be effective in improving the effectiveness and efficiency of flood  
298 forecasting. Therefore, the determination of the nonlinear relationship of the water storage ratio curve under  
299 different geographical scenarios will provide new ideas for simulation and early warning of flash floods.

### 300 **Authors' contributions**

301 **Yulong Zhu:** Conceptualization, Methodology, Software, Validation, Formal Analysis, Investigation, Data

302 Curation, Writing-Original draft, Writing - Review & Editing.

303 **Yang Zhou:** Methodology, Validation, Investigation, Resources, Data Curation.

304 **Xiaorong Xu:** Methodology, Investigation, Data Curation.

305 **Changqing Meng:** Validation, Investigation, Data Curation.

306 **Yuankun Wang:** Conceptualization, Methodology, Writing-Original draft, Writing - Review & Editing,

307 Supervision, Project administration, Funding acquisition.

308

### 309 **Availability of data and materials**

310 The datasets used and/or analyzed during the current study are available from the corresponding author on

311 reasonable request.

312

### 313 **Competing interests**

314 The authors declare that they have no conflict of interest.

315

### 316 **Acknowledgments**

317 This study was supported by the National Natural Science Fund of China (52279064, 52209087), and the

318 Fundamental Research Funds for the Central Universities of China (2024MS069, 2024MS068).

319

### 320 **References**

321 Abbott, M. B., Bathurst, J. C., Cunge, J. A., O'Connell, P. E., and Rasmussen, J.: An introduction to the

322 European Hydrological System-Systeme Hydrologique Europeen, "SHE", 1: History and philosophy of

323 a physically-based, distributed modelling system. *Journal of Hydrology*, 87(1-2), 45-59,

324 [https://doi.org/10.1016/0022-1694\(86\)90114-9](https://doi.org/10.1016/0022-1694(86)90114-9), 1986.

325 Almazroui, M.: Rainfall trends and extremes in Saudi Arabia in recent decades. *Atmosphere*, 11(9), 964,  
326 <https://doi.org/10.3390/atmos11090964>, 2020.

327 Arnold, J. G., and Williams, J. R.: Validation of SWRRB: Simulator for water resources in rural basins. *J.*  
328 *Water Resour. Plan. Manage.* ASCE, 113(2), 243-256,  
329 [https://doi.org/10.1061/\(ASCE\)0733-9496\(1987\)113:2\(243\)](https://doi.org/10.1061/(ASCE)0733-9496(1987)113:2(243)), 1987.

330 Beven, K. J. and Kirkby, M. J.: A Physically Based Variable Contributing Area Model of Basin Hydrology.  
331 *Hydrological Sciences Bulletin*, 24, 43-69, <https://doi.org/10.1080/02626667909491834>, 1979.

332 Bevacqua, E., Vousdoukas, M. I., Zappa, G., Hodges, K., Shepherd, T. G., Maraun, D., Mentaschi, L., and  
333 Feyen, L.: More meteorological events that drive compound coastal flooding are projected under  
334 climate change. *Communications Earth & Environment*, 1(1), 47,  
335 <https://doi.org/10.1038/s43247-020-00044-z>, 2020.

336 Cabré, A., Remy, D., Marc, O., Burrows, K., and Carretier, S.: Flash floods triggered by the 15-17th March  
337 2022 rainstorm event in the Atacama Desert mapped from InSAR coherence time series. *Natural*  
338 *Hazards*, 116(1), 1345-1353, <https://doi.org/10.1007/s11069-022-05707-y>, 2023.

339 Cai, W., Borlace, S., Lengaigne, M., van Rensch, P., Collins, M., Vecchi, G., Timmermann, A., Santoso, A.,  
340 McPhaden, M. J., Wu, L., England, M. H., Wang, G., Guilyardi, E., and Jin, F. F.: Increasing frequency  
341 of extreme El Niño events due to greenhouse warming. *Nature Climate Change*, 4(2), 111-116,  
342 <https://doi.org/10.1038/nclimate2100>, 2014.

343 Camassa, R., Holm, D. D., and Hyman, J. M.: A new integrable shallow water equation. *Advances in Applied*  
344 *Mechanics*, 31, 1-33, [https://doi.org/10.1016/S0065-2156\(08\)70254-0](https://doi.org/10.1016/S0065-2156(08)70254-0), 1994.

345 Crawford, N. H. and Linsley, R. K.: Digital Simulation in Hydrology: Stanford Watershed Model IV.

346 Technical Report No. 39, Department of Civil Engineering, Stanford University, pp. 210, 1966.

347 Crossley, A., Lamb, R., Waller, S., and Dunning, P.: Fast 2D flood modelling using GPU technology-recent  
348 applications and new developments. In EGU General Assembly Conference Abstracts, p. 12043, 2010.

349 Fernández-Pato, J., Caviedes-Voullième, D., and García-Navarro, P.: Rainfall/runoff simulation with 2D full  
350 shallow water equations: Sensitivity analysis and calibration of infiltration parameters. *Journal of*  
351 *hydrology*, 536, 496-513, <https://doi.org/10.1016/j.jhydrol.2016.03.021>, 2016.

352 Hoch, J. M., Eilander, D., Ikeuchi, H., Baart, F., and Winsemius, H. C.: Evaluating the impact of model  
353 complexity on flood wave propagation and inundation extent with a hydrologic–hydrodynamic model  
354 coupling framework. *Natural Hazards and Earth System Sciences*, 19(8), 1723-1735,  
355 <https://doi.org/10.5194/nhess-19-1723-2019>, 2019.

356 Horton, R.: The role of infiltration in the hydrologic cycle. *Trans. Am. Geophys. Union* 14, 446-460,  
357 <https://doi.org/10.1029/TR014i001p00446>, 1933.

358 Hsu, P. C., Xie, J., Lee, J. Y., Zhu, Z., Li, Y., Chen, B., and Zhang, S.: Multiscale interactions driving the  
359 devastating floods in Henan Province, China during July 2021. *Weather and Climate Extremes*, 39,  
360 100541, <https://doi.org/10.1016/j.wace.2022.100541>, 2023.

361 Kim, J., Warnock, A., Ivanov, V. Y., and Katopodes, N. D.: Coupled modeling of hydrologic and  
362 hydrodynamic processes including overland and channel flow. *Advances in Water Resources*, 37,  
363 104-126, <https://doi.org/10.1016/j.advwatres.2011.11.009>, 2012.

364 Kirezci, E., Young, I. R., Ranasinghe, R., Muis, S., Nicholls, R. J., Lincke, D., and Hinkel, J.: Projections of  
365 global-scale extreme sea levels and resulting episodic coastal flooding over the 21st Century. *Scientific*  
366 *Reports*, 10(1), 11629, <https://doi.org/10.1038/s41598-020-67736-6>, 2020.

367 Kobayashi, K., Duc, L., Kawabata, T., Tamura, A., Oizumi, T., Saito, K., Nohara, D., and Sumi, T.: Ensemble

368 rainfall–runoff and inundation simulations using 100 and 1000 member rainfalls by 4D LETKF on the  
369 Kumagawa River flooding 2020. *Progress in Earth and Planetary Science*, 10(1), 1-22,  
370 <https://doi.org/10.1186/s40645-023-00537-3>, 2023.

371 Köhne, J. M., Wöhling, T., Pot, V., Benoit, P., Leguédois, S., Le Bissonnais, Y., and Šimůnek, J.: Coupled  
372 simulation of surface runoff and soil water flow using multi-objective parameter estimation. *Journal of*  
373 *Hydrology*, 403(1-2), 141-156, <https://doi.org/10.1016/j.jhydrol.2011.04.001>, 2011.

374 Lee, J., Perera, D., Glickman, T., and Taing, L. Water-related disasters and their health impacts: A global  
375 review. *Progress in Disaster Science*, 8, 100123, <https://doi.org/10.1016/j.pdisas.2020.100123>, 2020.

376 Li, M., and Yao, J.: Precipitation extremes observed over and around the Taklimakan Desert, China. *PeerJ*, 11,  
377 e15256, <https://doi.org/10.7717/peerj.15256>, 2023.

378 Li, P. W., and Fan, C. M.: Generalized finite difference method for two-dimensional shallow water equations.  
379 *Engineering Analysis with Boundary Elements*, 80, 58-71,  
380 <https://doi.org/10.1016/j.enganabound.2017.03.012>, 2017.

381 Liu, Z., Zhang, H., and Liang, Q.: A coupled hydrological and hydrodynamic model for flood simulation.  
382 *Hydrology Research*, 50(2), 589-606, <https://doi.org/10.2166/nh.2018.090>, 2019.

383 Merkuryeva, G., Merkuryev, Y., Sokolov, B. V., Potryasaev, S., Zelentsov, V. A., and Lektuers, A.:  
384 Advanced river flood monitoring, modelling and forecasting. *Journal of Computational Science*, 10,  
385 77-85, <https://doi.org/10.1016/j.jocs.2014.10.004>, 2015.

386 Merz, B., Blöschl, G., Vorogushyn, S., Dottori, F., Aerts, J. C., Bates, P., Bertola, M., Kemter, M., Kreibich,  
387 H., Lall, U., and Macdonald, E.: Causes, impacts and patterns of disastrous river floods. *Nature*  
388 *Reviews Earth & Environment*, 2(9), 592-609, <https://doi.org/10.1038/s43017-021-00195-3>, 2021.

389 Ming, X., Liang, Q., Xia, X., Li, D., and Fowler, H. J.: Real-time flood forecasting based on a

390 high-performance 2-D hydrodynamic model and numerical weather predictions. *Water Resources*  
391 *Research*, 56(7), e2019WR025583, <https://doi.org/10.1029/2019WR025583>, 2020.

392 Mori, K., Tada, K., Tawara, Y., Ohno, K., Asami, M., Kosaka, K., and Tosaka, H.: Integrated watershed  
393 modeling for simulation of spatiotemporal redistribution of post-fallout radionuclides: application in  
394 radiocesium fate and transport processes derived from the Fukushima accidents. *Environmental*  
395 *Modelling & Software*, 72, 126-146, <https://doi.org/10.1016/j.envsoft.2015.06.012>, 2015.

396 Najibi, N., and Devineni, N.: Recent trends in the frequency and duration of global floods. *Earth System*  
397 *Dynamics*, 9(2), 757-783, <https://doi.org/10.5194/esd-9-757-2018>, 2018.

398 Nanditha, J. S., Kushwaha, A. P., Singh, R., Malik, I., Solanki, H., Chuphal, D. S., Dangar, S., Mahto, S. S.,  
399 Vegad, U., and Mishra, V.: The Pakistan flood of August 2022: Causes and implications. *Earth's Future*,  
400 11(3), e2022EF003230, <https://doi.org/10.1029/2022EF003230>, 2023.

401 Petersen-Overleir, A.: Modelling looped rating curves. In *Proc., XXIV Nordic Hydrological Conf*, pp.  
402 139-146, <https://doi.org/10.13140/2.1.1069.4403>, 2006.

403 Ruidas, D., Saha, A., Islam, A. R. M. T., Costache, R., and Pal, S. C.: Development of geo-environmental  
404 factors controlled flash flood hazard map for emergency relief operation in complex hydro-geomorphic  
405 environment of tropical river, India. *Environmental Science and Pollution Research*, 30, 106951-106966,  
406 <https://doi.org/10.1007/s11356-022-23441-7>, 2022.

407 Sanders, B. F., Schubert, J. E., and Detwiler, R. L.: ParBreZo: A parallel, unstructured grid, Godunov-type,  
408 shallow-water code for high-resolution flood inundation modeling at the regional scale. *Advances in*  
409 *Water Resources*, 33(12), 1456-1467, <https://doi.org/10.1016/j.advwatres.2010.07.007>, 2010.

410 Sugawara, M.: The development of hydrological model-tank. *Time and the River: essays by eminent*  
411 *hydrologists.*, 201-258, 1995.

412 Tellman, B., Sullivan, J.A., Kuhn, C., Kettner, A. J., Doyle, C. S., Brakenridge, G. R., Erickson, T. A., and  
413 Slayback, D. A.: Satellite imaging reveals increased proportion of population exposed to floods. *Nature*,  
414 596, 80-86, <https://doi.org/10.1038/s41586-021-03695-w>, 2021.

415 Tradowsky, J. S., Philip, S. Y., Kreienkamp, F., Kew, S. F., Lorenz, P., Arrighi, J., ... and Wanders, N.:  
416 Attribution of the heavy rainfall events leading to severe flooding in Western Europe during July 2021.  
417 *Climatic Change*, 176(7), 90, <https://doi.org/10.1007/s10584-023-03502-7>, 2023.

418 Valente, M., Zanellati, M., Facci, G., Zanna, N., Petrone, E., Moretti, E., Barone-Adesi, F., and Ragazzoni, L.:  
419 Health system response to the 2023 floods in Emilia-Romagna, Italy: a field report. *Prehospital and*  
420 *Disaster Medicine*, 38(6), 813-817, <https://doi.org/10.1017/S1049023X23006404>, 2023.

421 Ward, P. J., Jongman, B., Kumm, M., Dettinger, M. D., Sperna Weiland, F. C., and Winsemius, H. C.:  
422 Strong influence of El Niño Southern Oscillation on flood risk around the world. *Proceedings of the*  
423 *National Academy of Sciences*, 111(44), 15659-15664, <https://doi.org/10.1073/pnas.1409822111>, 2014.

424 Wu, H., Chen, B., Ye, X. et al.: An improved calibration and uncertainty analysis approach using a  
425 multicriteria sequential algorithm for hydrological modeling. *Scientific Reports*, 11, 16954,  
426 <https://doi.org/10.1038/s41598-021-96250-6>, 2021.

427 Zhu, Y. L., Ishikawa, T., Subramanian, S.S., and Luo, B.: Simultaneous analysis of slope instabilities on a  
428 small catchment-scale using coupled surface and subsurface flows. *Engineering Geology*, 275, 105750,  
429 <https://doi.org/10.1016/j.enggeo.2020.105750>, 2020.

430 Zhu, Y. L., Zhang, Y. F., Yang, J., Nguyen, B. T., and Wang, Y.: A novel method for calculating distributed  
431 water depth and flow velocity of stormwater runoff during the heavy rainfall events. *Journal of*  
432 *Hydrology*, 612, 128064, <https://doi.org/10.1016/j.jhydrol.2022.128064>, 2022.